The influence of alkyl ammonium modifiers on the microstructure and high-pressure rheology of sepiolite-vegetable oil dispersions

M.J. Martín-Alfonso, A. Mejía, F.J. Martínez-Boza*, P. Partal

Centro de Investigación en Tecnología de Procesos y Productos Químicos. (Pro2Tecs). Escuela Técnica Superior de Ingeniería, Universidad de Huelva. Avda. Tres de Marzo s/n, Huelva (Spain)

*Corresponding author: martinez@uhu.es

Abstract

In the context of environmental sustainability, the drilling industry faces new challenges resulting in the study and development of new drilling fluids based on eco-friendlier components to replace harmful mineral oils. Organic modified sepiolite dispersed in oil is an excellent additive to provide suitable rheological properties at low concentrations. The present study investigates the effect of alkyl ammonium modifiers on the microstructure and rheological properties of sepiolite-vegetable oil dispersions under high-temperature (up to 140ºC) and high-pressure (up to 2000 bar) conditions. Organo-sepiolite, prepared using a high-shear processing method and containing surfactant with alkyl chains longer than 12 carbon atoms, exhibited a high degree of surface adsorption and thermal resistance. All modifiers developed a stable fibrous structure in the dispersion. This structure maintained the pseudoplastic behavior in a wide range of shear rate, temperature and pressure without reaching an apparent yield stress. These dispersions showed suitable rheological and thermal properties to develop sustainable drilling fluids.

Keywords: sepiolite, alkyl-ammonium, vegetable oil, drilling fluid, high-pressure rheology

1 Introduction

The growing demand for energy and the excessive dependence on fossil fuels have created major environmental problems given the excessive production of greenhouse gasses and the resulting global climate change. This situation has forced the exploration and development of new technologies that are based on environmentally friendly alternatives, such as solar and geothermal energy (Mohamed et al., 2021). In the context of environmental sustainability, the drilling industry faces new challenges resulting in the study and development of environmentally-friendly drilling fluids for the new demands, such as geothermal energy recovery and deep storage of CO_2 (Ahmed et al., 2021).

It is well known that one of the most important properties of drilling fluids is a suitable rheology (high viscosity at low shear rate and low viscosity at high shear rate) (Caenn et al., 2017). Water-based drilling fluids (WBDFs) are environmentally more efficient than oil-based drilling fluids (OBDFs) (Amani et al., 2012; Reinoso et al., 2019, 2020). However, OBDFs are preferred for challenging deeper drilling scenarios having aggressive high-pressure and high-temperature conditions (HPHT) (Hermoso et al., 2015).

Fibrous and layered clay minerals are excellent additives that provide suitable rheological properties for drilling fluids even at low concentrations. Sepiolite has been used as a rheology improver and a fluid-loss controller in WBDFs (Tunç et al., 2012; Abdo et al., 2016; Ettehadi et al., 2020; Zhang et al., 2020). For OBDFs, organoclay (OC) is easily dispersible in oils, providing a dispersion that results in fluids having the desired pseudoplasticity and gel strength. Organo-sepiolites (OSep) provide dispersion with rheological properties that are like other layered OC such as organo-montmorillonites

(OMt) at lower loads. The fibrous structure and high aspect ratio of OSep improve interactions between clay and oil, as well as clay to clay, resulting in the development of percolated structures that exhibit pseudoplastic behavior. Surface modification is the key factor on how OC and oils interact, providing them compatibility and emulsifying capability (Lagaly et al., 2006).

Raw sepiolite (Sep) has been extensively surface-modified using different processing conditions, compounds and solvents (García et al., 2010; Mejía et al., 2014; Tiemblo et al., 2015). Adsorption of the modifier on the Sep surface can occur at distinct sites: a) oxygen ions on the tetrahedral sheet of ribbons, b) water molecules coordinated to the Mg ions and c) SiOH groups along the fiber axis (Serratosa, 1979). Sep has a low cation exchange capacity (CEC) ranging from 10 to 30 cmol(+)/kg (Aranda et al., 2008). Nevertheless, it can adsorb more than 4 times its CEC (Shariatmadari et al., 1999; Bilgiç, 2005).

OBDFs formulated with OSep and mineral oils have been tested in several works (Weng et al., 2018; Zhuang et al., 2018a, 2018b, 2018c, Zhuang et al., 2019). It is agreed that surface adsorption of the surfactant is the main mechanism for surfactant-clay interaction. Clay-oil compatibility and rheological properties are proportional to surfactant concentration. However, extremely high surfactant levels may result in a decline in rheological properties. Improved adhesion has been observed for cationic surfactants with long chains.

Recently, the rheological properties and structure of OC dispersed in vegetable-based solvents have been studied (Agwu et al., 2015; Ratkievicius et al., 2017; Sulaimon et al., 2017; Martín-Alfonso, 2021a), with promising results on the development of drilling products. As an advantage, vegetable oils provide a cheap and environmentally friendly alternative to replace the typically used environmentally harmful oils in OBDF

(Tapavicza, 2005; Li et al., 2016; Paswan and Mahto, 2020). Some thermal disadvantages related to oil resistance and degradation have recently been addressed (Ma et al., 2022; de Brito Buriti et al., 2022).

To expand on this, it may be necessary to conduct rheological studies under high pressure conditions applied to OSep dispersions formulated with vegetable oils to assess the capacity of these dispersions for designing eco-friendlier drilling fluids. A prior study revealed the suitability of certain vegetable oils, especially sunflower oil, as potential oily bases for the preparation of drilling fluids based on commercial OSep, showing excellent stability under high temperature/high pressure conditions (Martín-Alfonso et al., 2021a). This research expands upon the study of the structure and rheological behavior, as a function of temperature and pressure, of OSep dispersions in vegetable oils, prepared with different alkyl ammonium surfactants using a high-shear wet method. The novelty lies in assessing the impact of alkylammonium surfactants on the structure and pressure-temperature rheology of OBDFs prepared by dispersing OSep in vegetable oil.

2 Materials and methods

2.1 Materials

Sep (Pangel S9) donated by TOLSA (Spain) was used as a base product to prepare OSep through cationic exchange with different alkylammonium surfactants. This Sep is an industrially processed product (Alvarez Berenguer et al., 1985) with a cation exchange capacity (CEC) of 30 cmol(+)/kg (García-López et al., 2010).

Surfactants with different molecular weight and chain length were purchased from Sigma-Aldrich. The selected surfactants were tetrabutylammonium bromide (TBA-Br, molar mass 322.37 g/mol), dodecyl trimethylammonium bromide (DDTA-Br molar mass

308.34 g/mol), and hexadecyl trimethylammonium bromide (HDTA-Br molar mass 364.45 g/mol).

Crude vegetable sunflower oil was provided by LIPSA (Spain) and was used without modification to prepare OSep dispersions. A commercial OSep (Berkbent SB-5), prepared at industrial scale with an alkyl ammonium cationic surfactant was donated by TOLSA (Spain) and was used as reference OSep for comparison.

2.2 Processing

Sep was modified by cationic exchange using a high-shear wet method. Sep was dispersed in deionized water at 4 m% by means of a high shear mixer (Silverson). Then, a specific amount of surfactant (30 cmol(+)/kg of Sep), previously dissolved in 100 ml of water, was poured in the sepiolite-water dispersion and was agitated at 9000 rpm for 1h. Afterward, the liquid was separated by filtration and the solid was dried in an oven at 105°C, milled and dried again overnight. The theoretical composition of these organo-sepiolites is shown in Table 1.

Table 1. Formulation of OSep samples

		4 m% sepiolite/water dispersion		
OSep	Modifier	Water (g)	Sepiolite (g)	Modifier (g)
ST30	Tetrabutylammonium bromide	2500	100	9.67
SD30	Dodecyl trimethylammonium bromide	2500	100	9.25
SH30	Hexadecyl trimethylammonium bromide	2500	100	10.93

OSep dispersions in oil were formulated at a concentration of 3 m% by wetting with the vegetable oil in a low shear mixer, using a conventional four-blade impeller for two hours at room temperature. Afterward, the OSep dispersions were high shear mixed using an Ultra-Turrax T50 high-performance dispersing machine (Ika, Germany) at the temperature of 60ºC and at 12000 rpm for ten minutes.

The samples were stored in closed containers at room temperature. Before the testing, the samples were homogenized in a low shear mixer for five minutes, observing no separation phase.

2.3 Methods

XRD characterization was conducted at room temperature, using a Bruker S8 Advance diffractometer (Germany) equipped with a secondary monochromator, a Brentano Bragg geometry goniometer and a copper cathode as an X-ray source. Samples were exposed to Cu Kα radiation at a wavelength of 0.15406 nm. The 2θ angles ranged from 1.5º to 40º, with a 0.017º single scanning step and a measurement time of 6 seconds per step.

OSep morphologies were observed on a Jeol JSM-5410 scanning electron microscope (20 kV and 20,000x), using samples coated with gold at high vacuum to avoid charging.

Fourier Transform Infrared (FTIR) spectra of the studied samples were obtained using a Jasco FTIR-4200LE spectrometer. FTIR spectra were recorded in the 4000 to 400 cm^{-1} range in transmission mode. Solid samples were mixed with potassium bromide (KBr) at a ratio of approximately 1/10 weight and were pelletized in a hydraulic press at 50 bars.

Calorimetric analyses were performed using an MDSC-Q100 (TA Instruments). Samples consisting of 5-15 mg were sealed in aluminum pans and were purged with N_2 at 50 mL/min. Temperature scans were conducted between -80°C and 250°C, with an oscillation period of 60 seconds, an amplitude of 0.50°C, and a heating rate of 5°C/min.

Thermogravimetric analyses were conducted on a TGA-Q50 (TA Instruments) under N_2 flow. Samples were isothermally stabilized at 55ºC for five minutes and were subsequently heated to 600ºC, at a heating rate of $10ºC \cdot min^{-1}$ for Sep and OSep and $20ºC \cdot min^{-1}$ for oil dispersions.

Rheological measurements were taken using controlled-stress rheometers (Haake Mars II, Thermo Scientific and MCR301, Anton Paar). Rheological data were obtained at atmospheric pressure using standard coaxial cylinder geometry (DINZ20 and CC27, gap 1 mm).

Pressure–temperature flow curves were obtained using a non-conventional coaxial cylinder-type pressure cell (HP2000) equipped with a magnetically-coupled coaxial cylinder (inner diameter 26 and 27 mm, gap 1 mm and 0.5 mm, respectively).

Viscosity-pressure ramps were performed using a patented high-pressure flow driven capillary viscometer, equipped with a high-pressure opposed-piston pump, pressure generators and a set of high-pressure capillaries enclosed in a climate chamber. Details of this device have been reported elsewhere (Martín-Alfonso et al., 2021b).

Steady-state flow curves were measured at several temperature and pressure combinations (40ºC, 60ºC, 80ºC, 100ºC, 120ºC and 140ºC at 1 bar and 40ºC, 100ºC and 140ºC at 500 bar, 1000 bar and 1500 bar), using upward stress sweep tests, in 180-second steps.

Viscosity versus pressure ramps were measured at 40ºC, 60ºC, 80ºC, 100ºC, 120ºC and 140ºC, at a high shear rate, increasing/decreasing pressure by ~250 bar steps, using high-pressure generators (Isco-Teledyne and HiP, USA) and the samples as pressurizing fluid. No significant hysteresis was observed when comparing upward and downward pressure sweeps.

3 Results and discussion

3.1 Structural characterization

As seen in Figure 1, the XRD patterns of the OSep dispersions are very similar to those of Sep. It is well known that the presence of organic modifiers does not alter the

crystalline structure of Sep due to the covalent bonds between the sheets. Therefore, the main reflections in Sep (2θ values 7.4º; 11.7º; 13.3º; 19.8º; 20.6º; 23.8º; 26.7º and 35) also appear in OSep and its dispersions, as previously reported in several works (García-López et al., 2010; Weng et al., 2018; Zhuang et al., 2018a, 2018b; Martín-Alfonso et al 2021a). The dispersions reveal an increase in the intensity at the 15º-26º 2θ range with respect to Sep and OSep. This effect is related to the adsorption of the organic oil phase as reported previously by Yan et al. (2016). Amorphous adsorption of the organic surfactants on the surface may be the dominant interaction mechanism in OSep (Weng et al., 2018), with no effect of the type of alkyl ammonium salt, chain length or the organic dispersant oil (Zhuang et al., 2018a).

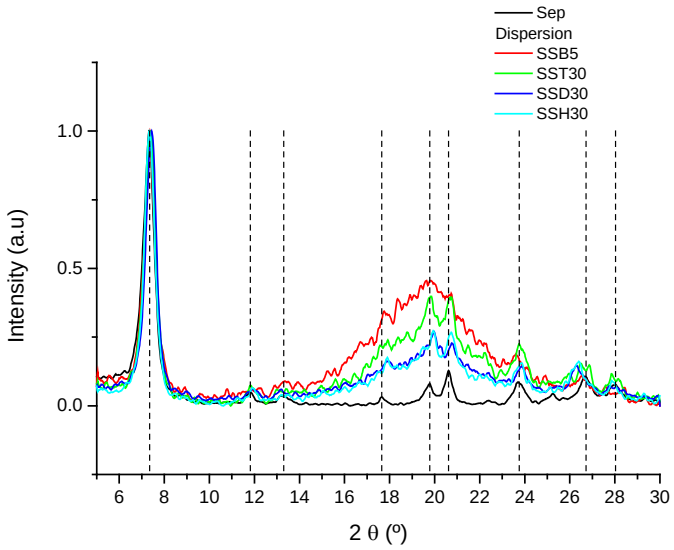

Figure 1. XRD patterns of the Sep and OSep dispersions SSB5, SST30, SSD30 and SSH30 in vegetable oil.

FTIR can provide insight into the adsorption properties of surfactants. In this sense, the FTIR spectra of Sep and OSep are shown in Figure 2 in the 4000–400 cm^{-1} range. Sep shows a broad absorption band in the range 3700-3000 cm^{-1}. This result is consistent with literature (Tunç et al., 2011). The band at 3680±5 cm^{-1} belongs to the MgOH stretching

192 and is not affected by the presence of the surfactant in OSep samples (Aznar et al., 1992;
193 Rytwo et al., 1998). The bands at 3564 and 3416 cm^{-1}, corresponding to coordination
194 water stretching, are affected by the presence of adsorbed surfactant. The band at 3564
195 cm^{-1} is slightly shifted to higher wavenumbers (Karataş et al., 2013), while the band at
196 3416 cm^{-1} decreases in intensity and is shifted to higher wavenumbers for the SB5 sample
197 and is shifted to lower wavenumbers for the OSep samples prepared (Ruiz-Hitzky, 2001).
198 In the same sense, the band at 1665 cm^{-1} of Sep, corresponding to the bending vibration
199 of OH, is displaced to 1622 cm^{-1} for SB5 and 1668 cm^{-1} for all prepared OSep samples,
200 indicating that, in both cases, the surfactant is mainly adsorbed on the Sep surface. Similar
201 results were obtained by other authors using Turkey sepiolites modified with similar
202 surfactants (Tunç et al., 2011; 2012). Asymmetric C-H stretching appears in the OSep at
203 2938, 2964, 2927 and 2927 cm^{-1} and symmetric C-H stretching at 2854, 2876, 2856 and
204 2854 cm^{-1}, for samples SB5, ST30, SD30 and SD30, respectively. The band at 1211 cm^{-1}
205 , corresponding to asymmetric Si-O-Si stretching in Sep, is not displaced in the prepared
206 OSep and is shifted to lower wavenumbers (1195 cm^{-1}) only for commercial SB5. Finally,
207 the band of symmetric Si-O stretching at 1012 cm^{-1} is shifted to higher wavenumbers for
208 all OSep samples tested (1021 cm^{-1} for OSep SB5 and 1018 cm^{-1} for ST30, SD30 and
209 SD30).
210

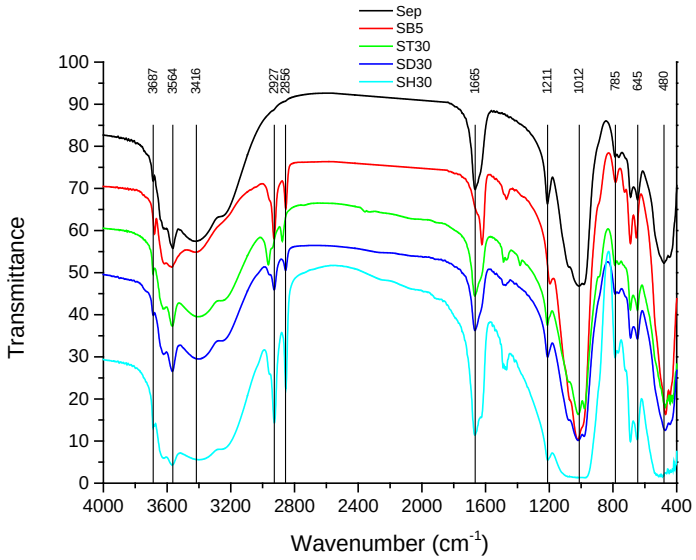

211

212 Figure 2. FTIR spectra of the examined OSep samples.

213

214 SEM surface morphology of OSep is displayed in Figure 3. All OSep samples reveal the
215 characteristic morphology of fibrous aggregates, similar to those previously reported in
216 the literature (García-López et al., 2010; Abdo et al., 2016; Zhuang et al., 2017, 2018a).
217 Some aggregation of the sepiolite's needles is observed due to the surfactant's coverage
218 of the surface. The SEM images show similar morphologies for the OSep samples that
219 were prepared with surfactants of different chain length and type.

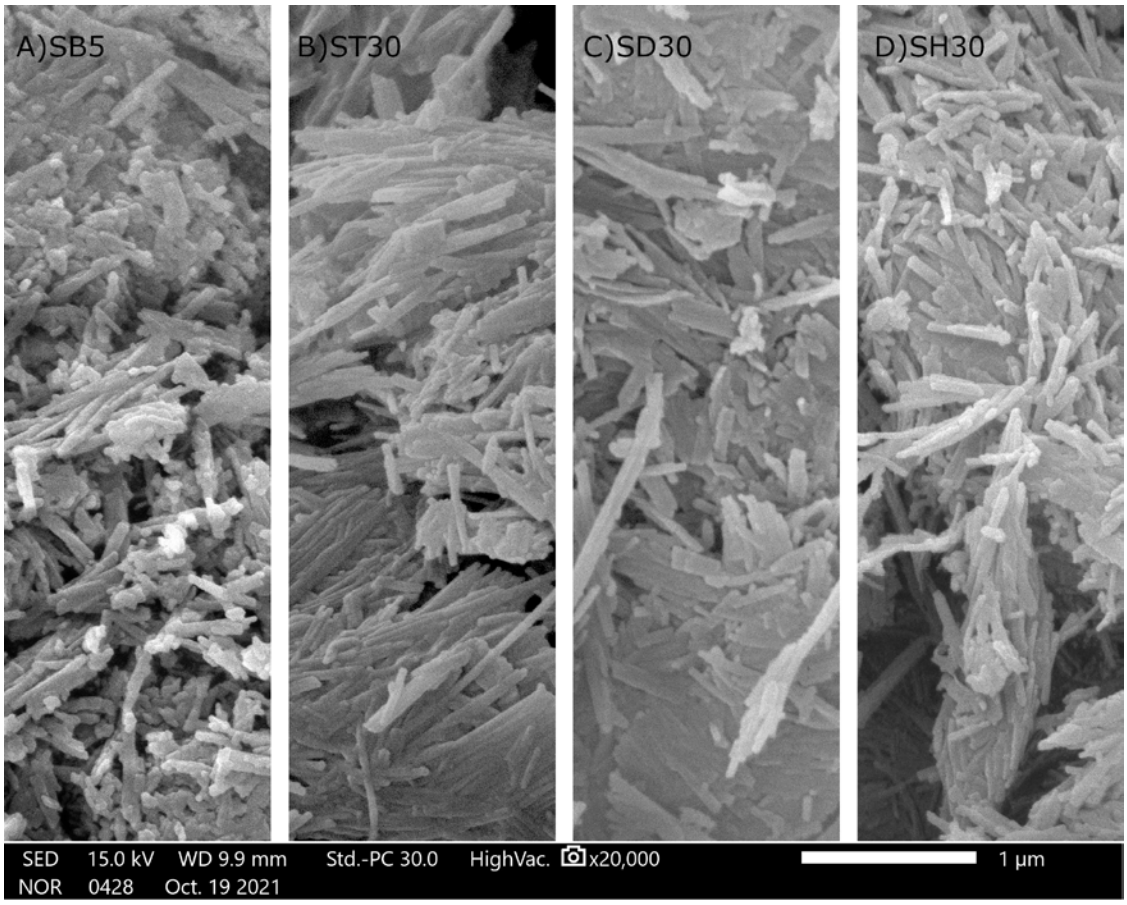

Figure 3. SEM images of the examined OSep samples. A) SB5; B) ST30; C) SD30; and D) SH30.

3.2 Thermomechanical characterization

Figure 4 shows the MDSC heating and cooling curves of the dispersions studied. All the prepared dispersions reveal an extensive endothermic melting in the reversing heat flow curve, characterized by an onset temperature of approximately -41ºC, quite similar to that of the base oil (see Table 2). The reversing heat flow curves show up to three melting peaks, the first of which was assigned to the first melting peak of the base oil (~-37ºC). This peak is slightly shifted to higher temperatures for the SSB5, SST30 and SSH30 samples. The second peak appears at -28ºC and corresponds to the main melting of the oil. For the OSep dispersions, this peak is divided into two peaks, a second one at

233 approximately -28ºC and a third at a higher temperature (~25ºC). This indicates that OSep
234 adsorbs some low molecular weight components of the oil, promoting compatibility and
235 shifting the melting of the wax components to higher temperatures. On the other hand,
236 the melting enthalpy of the OSep dispersions is significantly lower than that of the oil
237 (see Table 2), indicating that the oil adsorption and the interactions with the covered
238 surface influence the melting process of the oily components, increasing the amorphous
239 fractions of the dispersion. The addition of surfactants in OSep dispersions resulted in a
240 greater increase of the amorphous fraction, mostly in SST30 prepared with
241 tetrabutylammonium and to a lesser extent in SSH30, prepared with
242 hexadecylammonium. No correlation was found between chain length and the amorphous
243 fraction.
244

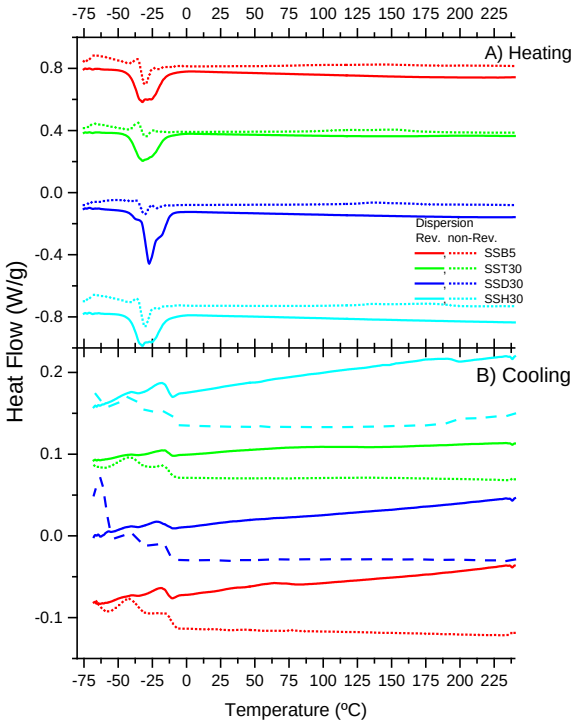

245

246 Figure 4. Heating and cooling curves from MDSC for the OSep dispersions studied.

The non-reversing signal reveals two thermal events at low temperatures: a cold crystallization event that is characterized by an exothermic peak related to the diffusion and assembly of hydrocarbon structures and the endotherm corresponding to the melting of saturates and waxes.

The reversible cooling curves, Fig. 4B, reveal extensive exothermic crystallization with a cloud point of approximately -8ºC (see Table 2, onset of the first peak), associated with the onset of incipient crystallization of higher molecular weight waxes; a first crystallization peak (pk1), at approximately -16ºC, associated with the formation of microcrystals of the oil's wax components; and a second peak (pk2), at approximately -40ºC, associated with the formation of polymorphic structures due to recrystallizations and microcrystal arrangements (Adhvaryu et al., 2002). It is likely that the melting of the phases due to polymorphic structures is responsible for the peak splitting and minor changes observed in the melting of OSep dispersions as compared to those of the oil discussed above. In agreement with the results from melting, the enthalpy of crystallization of the peak 1 resulted lower than that of the oil, mainly for the SST30 dispersion. The enthalpy of crystallization increases with the chain length, reaching values of 5.2 J/g for dispersions prepared with surfactants containing more than 12 carbon atoms and the commercial surfactant SB5.

Table 2. MDSC events for the samples under study.

	Crystallization				Melting				
	ºC			J/g	ºC				J/g
	Onset	Peak 1	Peak 2	ΔH_{c1}	Onset	Peak 1	Peak 2	Peak 3	ΔH_m
Oil	-7.0	-15.2	-41.2	7.2	-42.7	-35.9	-27.7		74.62
SSB5	-8.7	-17.1	-39.4	5.3	-41.3	-32.8	-28.5	-26.0	47.03
SST30	-6.9	-14.8	-39.8	3.8	-42.6	-32.1	-28.5	-25.6	40.44
SSD30	-9.4	-16.6	-40.8	5.2	-41.3	-36.0	-27.2	-19.0	52.33
SSH30	-7.0	-15.2	-39.5	5.1	-41.2	-32.2	-28.6	-25.8	47.09

These results suggest that the thermal properties of OBDFs formulated with OSep and vegetable oils depend mainly on the properties of the oil, but also on interactions between the oil and the clay-modifying surfactant (Martín-Alfonso, et al. 2021a).

TGA results are shown in Figure 5 and Table 4. Sep presents a mass loss of 7.21% due to the surface water (room temperature -150ºC range). The mass loss attributed to zeolitic and coordinated water is 4.91%, occurring in the intervals 150ºC - 320ºC and 320ºC - 595ºC, which are mass losses of 2.66% and 2.25% respectively (Tartaglione et al., 2008; Frost and Ding, 2003).

The mass loss in the temperature interval below 150ºC is 6.18%, 2.76% and 1.88% for the OSep ST30, SD30 and SH30 samples, respectively. This mass loss is mainly due to the decrease in surface water content, as the surfactant does not show any significant mass loss within this temperature range as seen in Table 3.

Table 3. Temperature for characteristic mass loss of the surfactants studied.

	$T_{1\% \text{ mass loss}}$ (ºC)	$T_{5\% \text{ mass loss}}$ (ºC)	$T_{10\% \text{ mass loss}}$ (ºC)	$T_{50\% \text{ mass loss}}$ (ºC)	$T_{100\% \text{ mass loss}}$ (ºC)
TBA-Br	174.66	187.08	193.57	214.94	255.54
DDTA-Br	198.73	222.6	232.27	259.32	284.83
HDTA-Br	201.16	223.49	232.98	259.96	291.23

The surface water content of 6.19% calculated from TGA for the OSep ST30 sample is very close to that measured for Sep. This would indicate a low degree of TBA adsorption on the surface of Sep mineral, resulting a heterogeneously coverage of the surface and poor hydrophobic properties (Weng et al., 2018; Zhuang et al., 2018b). This contrasts with the good stability and rheological properties observed for the dispersion formulated with OSep ST30. This suggests that processing has a major influence on the final dispersion properties.

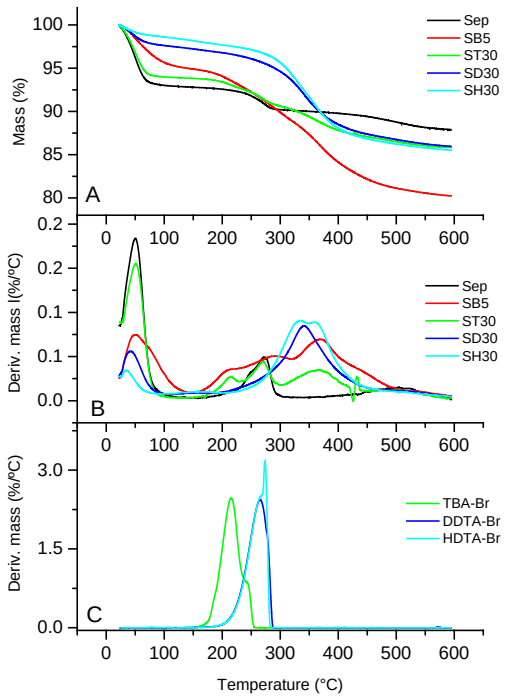

290

291 Figure 5. TGA thermograms for Sep, OSep and surfactant samples. A) Sep, OSep SB5,
292 ST30; SD30 and SH30. B) Derivative of mass loss (DTG) of Sep, OSep SB5, ST30; SD30
293 and SH30. C) Derivative of mass loss of the surfactants TBA, DDTA and HDTA.

294

295 Both structural water loss and surfactant degradation occur in overlapped stages in the
296 150ºC-590ºC interval, with mass losses of 14.64%, 7.96%, 11.24%, 12.63% for OSep
297 SB5, ST30, SD30 and SH30, respectively. Based on these results, the water content of
298 dry Sep was estimated to be 5.59 g/100 g. Therefore, the surfactant content based on the
299 dry Sep can be estimated as seen in Table 4, if a similar mechanism occurs in the
300 organoclay for the dehydration process.

301 Table 4. Mass loss and surfactant concentration for Sep and OSep from TGA

	Mass				Calculated amount of modifier	
Sample	m% at 150ºC	m% H_2O	m% at 590 ºC	m% H_2O+Surf	g/100 g folded Sep	g/100 g dry Sep
Raw Sep	92.79	7.21	87.88	4.91	-	-

SB5	94.90	5.1	80.26	14.64	12.65	11.98
ST30	93.81	6.19	85.85	7.96	3.68	3.49
SD30	97.22	2.78	85.98	11.24	7.49	7.09
SH30	98.17	1.83	85.54	12.63	9.18	8.69

The derivative of mass loss (DTG) is displayed in Figure 5B. OSep ST30 reveals up to three stages for the surfactant decomposition in the range of temperature 150-595ºC. The first stage shows a maximum in the DTG curve at 215ºC. This temperature corresponds to the maximum observed in the derivative of mass loss for pure TBA-Br, as seen in Figure 5C. Therefore, it could be associated with the decomposition of a small amount (less than 1% mass loss) of free or weak adsorbed surfactant. The second stage has a maximum at 290ºC and a minimum at 303ºC (close to the final decomposition temperature of the pure TBA-Br, see Table 3). At this stage, 3.24% of the mass loss corresponds to zeolitic water and surfactant decomposition. Since zeolitic water is blocked into channels and tunnels covered by the surfactant, a large portion of the mass loss corresponds to the surfactant (Zhuang et al., 2018a). The third stage occurs in the 303-595ºC range with a total mass loss of 4.76% (TBA surfactant and structured water) of which 2.51% corresponds to surfactant adsorbed mainly on the channel due to the shifting of the decomposition temperature beyond the temperature range where the pure surfactant decomposition occurs.

The decomposition of OSep SD30 and SH30 occurs in a unique stage over a wide range of temperature, from 150 to 590ºC. Sample SD30 shows a broad maximum at 341ºC in the derivative of the mass loss curve. This temperature is significantly higher than that found for the pure surfactant DDTA-Br, indicating that the decomposition of the adsorbed surfactant is shifted significantly to higher temperatures, probably due to a high degree of adsorption on the channels. In addition, at 284ºC, the final temperature of the decomposition of the pure DDTA-Br, a large amount of DDTA remains adsorbed by Sep,

equivalent to 6.96% of the mass loss. Similar results were found for SH30, as found by other authors (Weng et al., 2018), with a divided maximum in the derivative at 334 and 360ºC, and a remaining 8.33% of the surfactant at the final decomposition temperature of the pure DHTA-Br. The shifting of the surfactant decomposition to higher temperatures relates to a large degree of adsorption on the channels and tunnels (Zhuang et al., 2018a). In this case, however, the results from the FTIR do not reveal evidence of surfactant penetration in the tunnels (Ruiz-Hitzky, 2001). The decomposition of the surfactant in a broad stage is related to greater effectivity in the adsorption due to the effectiveness of the high shear processing during OSep preparation. Similar results were obtained by Zhuang et al. (2017), processing OPal with high-shear mixers.

The thermal stability of the OSep has been analyzed with the aid of TGA, and the resulting temperature at mass loss of 1%, 5% and 10% are displayed in Table 5. OSep dispersions show high thermal resistance with temperatures at 1% mass loss of 305.7ºC, 305.ºC, 298.3ºC, and 313.4ºC for OSep SB5, ST30; SD30 and SH30, respectively. These temperatures are slightly lower than that of the vegetable oil due to the overlapping of mass loses related to both the dehydration water and the surfactant decomposition (Martín-Alfonso et al., 2021a). Thus, the temperatures for the 5% and 10% mass losses are closer to that corresponding to the mass loss of the oil, suggesting that the properties of the continuous oil phase determine the thermal resistance of the dispersion. However, the temperatures at which the maximum appears for the derivative of mass are higher for the OSep dispersions than for the oil. This reveals the positive influence of the dispersed phase on the dispersion's thermal resistance. This effect increases slightly with the chain length.

Table 5. TGA thermograms of vegetable oils and OSep dispersions.

	Degradation Temperatures (ºC)			
Samples	$T_{1\%\ mass\ loss}$ (ºC)	$T_{5\%\ mass\ loss}$ (ºC)	$T_{10\%\ mass\ loss}$ (ºC)	T_{peak} (ºC)
Oil	331.02	372.41	387.1	425.98
SSB5	305.69	362.42	383.35	433.65
SST30	305.31	365.35	381.97	430.10
SSD30	298.29	364.41	383.44	432.94
SSH30	317.28	367.13	384.45	431.95

3.3 Rheological characterization

Figure 6 shows the steady-state flow curves for selected dispersions at 40ºC and atmospheric pressure. These dispersions behave as pseudoplastic fluids in the shear rate range tested. Pseudoplasticity is a required property in drilling fluids that prevents the settling of the cutting given the high viscosity values at low shear rate when the circulation is stopped. On the other hand, at high circulation rates, low viscosity values facilitate the rate of penetration of the bit, saving energy. Thus, these OSep dispersed in vegetable oil have suitable rheology to develop environmentally-friendly drilling fluid formulations.

From a structural point of view, OC particles dispersed in the Newtonian oil have a weak structure of associated aggregates at relatively low OC concentration (about 3 m% and higher, Hermoso et al., 2014a, 2014b). The associated dispersion is characterized by low apparent yield stress and high viscosity values, in the low shear rate regime. As the shear rate increases, the OC associations are disrupted and the weak structure gradually disappears, with a significant decrease in viscosity. Moreover, the orientation of the OSep particles in the direction of the flow results in a lower degree of interactions of the dispersed phase, with additional decreases in viscosity. And at higher shear rates, the dispersion tends to reach a limit in viscosity that is significantly higher than the

Newtonian viscosity of the oil's continuous phase. In this shear rate region, the minimum friction of the particles is oriented in the flow direction, lowering the viscosity with respect to the low shear region, but the remaining interactions in the oriented particles are responsible for the increased viscosity as compared to that of the oil. In this region, dispersion-oil viscosity ratio always increases with temperature, although less significantly for OSep modified with surfactants with longer alkyl chains (SSH30). This OSep would be more compatible with oil, leading to a lower contribution of the dispersed phase to bulk viscosity.

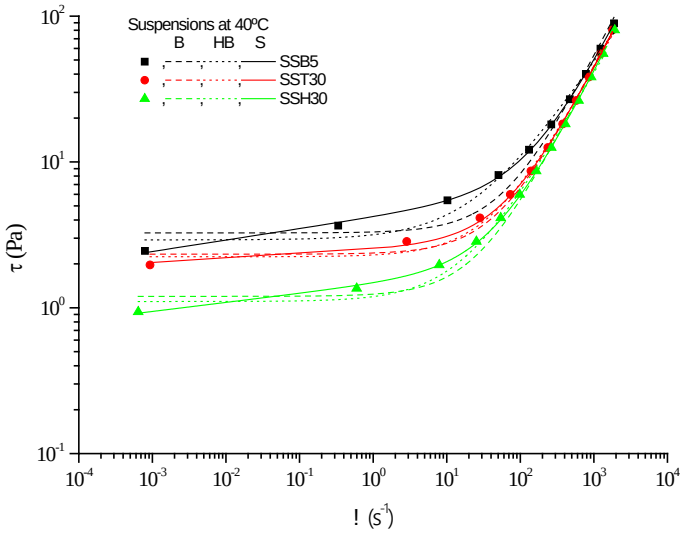

Figure 6. Comparative of the different models (B Bingham model, HB Herschel-Bulkley model, and S Sisko model) applied to the flow curves of selected dispersions. (Models parameters presented in Table S1 of supplementary material).

Classical equations frequently used to model the viscous flow behavior of drilling fluids (Agwu et al, 2021) such as Bingham, Herschel-Bulkley, and Sisko models (Eq 1, 2 and

3, respectively) have been tested to fit the viscoplastic behavior of the examined OSep dispersions. The results are displayed in Figure 6.

$$\tau = \tau_B + \eta_P \dot{\gamma} \quad (1)$$

$$\tau = \tau_H + k_0 \dot{\gamma}^{n_0} \quad (2)$$

$$\tau = \eta_\infty \dot{\gamma} + k_0 \dot{\gamma}^{n_0} \quad (3)$$

The Bingham model is one the simplest equation applied to drilling dispersions (Rossi et al., 2002) and predicts the rheological behavior using two fitting parameters, at low shear rate, the apparent Bingham yield stress, τ_B, and at high shear rates, the plastic viscosity η_p. Despite this, most drilling fluids are not exactly described by this model, as previously reported (Caenn et al., 2017; Hermoso et al., 2014b), this model is a powerful equation for engineering purposes.

The three-parameter Herschel-Bulkley model agrees much more closely with drilling fluid rheology, especially at low shear rates, accounting for the yielding behavior by the apparent Herschel-Bulkley yield stress, τ_H, and the non-linear relationship between shear stress and shear rate by power law, with the consistency index, k_0, and the flow index, n_0. These OC dispersions do not reveal a clear trend to reach an apparent yield stress. Both the Bingham and Herschel-Bulkley models fail mainly at intermediate and lower shear rates, overestimating the values of the apparent yield stress. Nevertheless, in some cases, thermomechanical aging tends to develop structures having a clearer tendency to reach an apparent yield stress. As seen in Figure 6, the Sisko model more accurately predicts the rheological behavior of the OC dispersion at low and intermediate shear rates. Nevertheless, for engineering purposes, the three models offer acceptable results in the high shear rate region.

At these concentrations, fibrillary OC are likely to develop a weak dispersed phase structure of connected needles (see Figure 3). This structure appears to be very sensitive to shear, when stress applied to the fibrillary aggregates changes their equilibrium positions to accommodate to the flow, when the applied stress increases the breakage of physical linkages occurs and when new ones are arranged in new equilibrium positions, forming new and weaker structures having less flow resistance, resulting in a decreased viscosity. The weak forces connecting the OSep needles are insufficient to maintain the structure and it does not develop a true yield stress like the laminar OC such as Organo-bentonite at the same concentration, in which the exfoliated layers form stronger percolating structures that in most cases which reveal a clear apparent yield stress (Hermoso et al., 2014b; Zhuang et al., 2019). In addition, the rheology of OSep dispersions is less affected by the surfactant chain length due to their non-swelling structure.

As seen in Figures 7-9, the Sisko model accurately describes the flow behavior of these dispersions at a wide range of temperatures and pressures. As expected, viscosity decreases with temperature and increases with pressure, but this increase is significantly lower than the decrease due to the temperature increase. However, the effect of temperature is dampened at high pressure due to the increase in molecular friction of the continuous phase components at higher pressures (Martín-Alfonso et al., 2021a; c). Coverage and chain length resulted in a decrease in the shear stress curves, probably due to the increased compatibility between the OSep and the oil.

The effect of pressure on the viscosity can be modelled using a factorial approach, such as the Sisko-Barus (Eq. 4 and 5) or Sisko-VTF (Eq. 4 and 6), as mentioned by the authors in previous publications (Hermoso et al., 2014a; Martín-Alfonso et al., 2021a; c). This approach separates the influence of pressure *(PF)* into two main contributions: the

influence on pseudoplasticity at low and intermediate shear rates, and the influence on bulk limiting viscosity at higher shear rates.

$$\tau = \left(\eta_\infty \cdot \dot{\gamma} + (k_0 + k_1(P - P_r)) \cdot \dot{\gamma}^{(n_0 + n_1(P - P_r))}\right) \cdot PF \qquad (4)$$

The effect of pressure at high circulation rates can be modelled from viscosity-pressure data measured at both a constant shear rate and a constant temperature, using a generalized Barus-like expression (Eq. 5), fitting the piezoviscous effect as a polynomial function of pressure.

$$PF = \exp\left(\beta_0(P - P_r) + \beta_1(P - P_r)^2\right) \qquad (5)$$

For these fluids, a second-grade polynomial function with two parameters, β_0 and β_1, accurately fits the experimental viscosity data measured at higher shear rates. Similarly, the VFT model can be also used to cover the entire range of temperatures and pressures tested with a temperature-pressure expression such as Eq. 6:

$$PF = exp\left(\frac{(B + b_1(P - P_r) + b_2(P - P_r)^2)}{(T - T_r) - C} + \frac{B}{C}\right) \qquad (6)$$

In OBDFs, the main contribution of pressure comes from the increased friction due to the compression of the continuous oil phase under pressure. This phenomenon leads to the increase in shear stress as is shown in Figures 8 and 9. Furthermore, at intermediates and lower shear rates the pseudoplastic behavior of the fluid under pressure can differ slightly from that predicted by the factorial model based on the piezoviscous contribution at high shear rates as compared to the flow curve measured at atmospheric pressure. This change in pseudoplasticity may be due to different interactions of the microstructure of the dispersed phase under the pressurized flow. Therefore, in this region the effect of pressure can be addressed by fitting linear functions of flow and consistency indexes, using the two parameters: n_1 and k_1. These parameters represent a correction of the effect of pressure, measured at high shear rates, over the shape of the pseudo plastic fall at

intermediate and lower shear rates, at a constant temperature. The results are presented in Table 6.

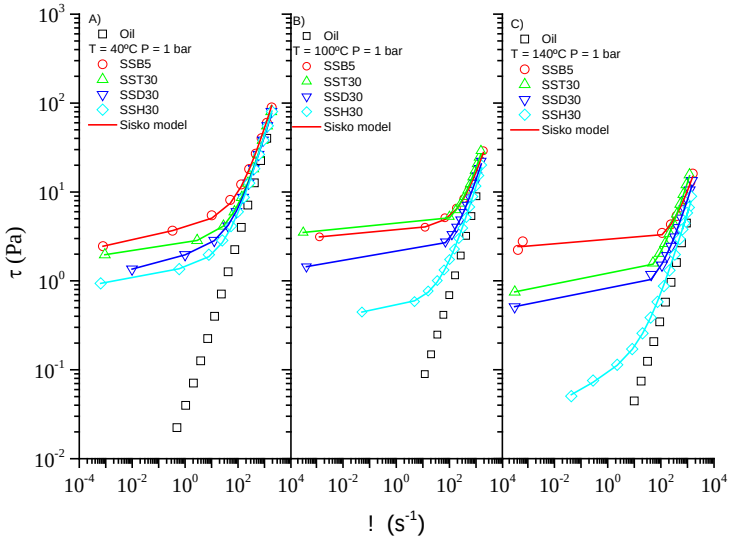

Figure 7. Steady state flow curves, at atmospheric pressure, as a function of temperature, for OBM formulated with 3 m% of OSep. A) 40ºC; B) 100ºC; C) 140ºC.

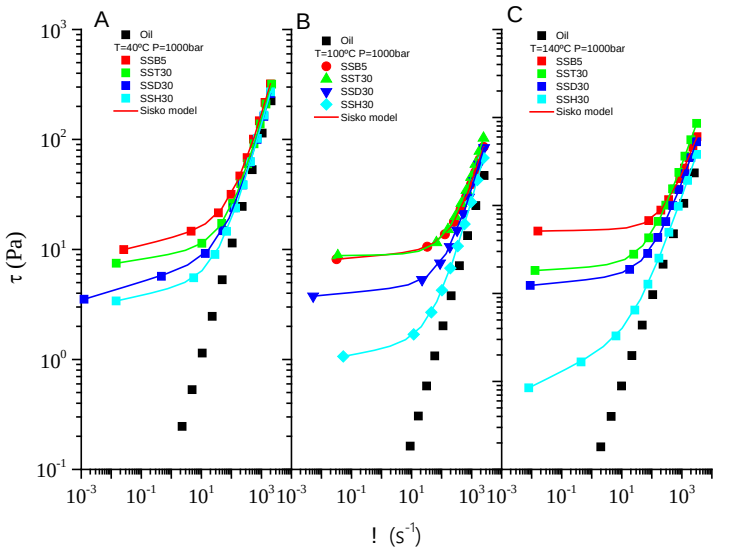

Figure 8. Steady state flow curves, at a pressure of 1000 bar, as a function of temperature, for OBM formulated with 3 m% of OSep. A) 40ºC; B) 100ºC; C) 140ºC.

466

467 Table 6. Parameters of the generalized Sisko model for the examined fluids.

SSB5						
	40ºC	60ºC	80ºC	100ºC	120ºC	140ºC
k_0 (Pa·s^n)	3.94	3.75	3.79	3.66	3.41	2.38
k_1 (Pa·s^n·bar^{-1})	$-3.00\cdot10^{-05}$			$-3.27\cdot10^{-05}$		$-1.18\cdot10^{-05}$
n_0	$6.63\cdot10^{-02}$	$4.81\cdot10^{-02}$	$3.04\cdot10^{-02}$	$2.24\cdot10^{-02}$	$1.14\cdot10^{-02}$	$0.58\cdot10^{-02}$
n_1 (bar^{-1})	$1.60\cdot10^{-06}$			$1.06\cdot10^{-06}$		$1.23\cdot10^{-06}$
η_∞ (Pa·s)	$4.56\cdot10^{-02}$	$2.68\cdot10^{-02}$	$1.74\cdot10^{-02}$	$1.21\cdot10^{-02}$	$9.12\cdot10^{-03}$	$7.60\cdot10^{-03}$
β_0 (bar)	$1.24\cdot10^{-03}$	$1.10\cdot10^{-03}$	$1.11\cdot10^{-03}$	$9.92\cdot10^{-04}$	$8.99\cdot10^{-04}$	$9.18\cdot10^{-04}$
β_1 (bar^{-2})	$-5.87\cdot10^{-08}$	$-5.41\cdot10^{-08}$	$-9.35\cdot10^{-08}$	$-7.73\cdot10^{-08}$	$-6.43\cdot10^{-08}$	$-9.30\cdot10^{-08}$
R^2	0.997	0.997	0.997	0.996	0.992	0.971
χ^2	$8.15\cdot10^{-4}$	$3.15\cdot10^{-3}$	$7.36\cdot10^{-4}$	$1.03\cdot10^{-3}$	$2.14\cdot10^{-3}$	$8.43\cdot10^{-3}$
SST30						
k_0 (Pa·s^n)	2.61	4.09	4.00	3.56	1.21	0.87
k_1 (Pa·s^n·bar^{-1})	$-3.49\cdot10^{-06}$			$-4.77\cdot10^{-06}$	-	$-43.93\cdot10^{-06}$
n_0	$4.07\cdot10^{-02}$	$0.80\cdot10^{-02}$	$0.28\cdot10^{-02}$	$0.23\cdot10^{-02}$	$0.30\cdot10^{-02}$	$1.91\cdot10^{-02}$
n_1 (bar^{-1})	$1.57\cdot10^{-06}$			$1.52\cdot10^{-06}$		$6.13\cdot10^{-07}$
η_∞ (Pa·s)	$4.04\cdot10^{-02}$	$2.42\cdot10^{-02}$	$1.87\cdot10^{-02}$	$1.51\cdot10^{-02}$	$1.34\cdot10^{-02}$	$1.17\cdot10^{-02}$
β_0 (bar^{-1})	$1.36\cdot10^{-03}$	$1.24\cdot10^{-03}$	$1.11\cdot10^{-03}$	$1.10\cdot10^{-04}$	$9.99\cdot10^{-04}$	$9.24\cdot10^{-04}$
β_1 (bar^{-2})	$-9.60\cdot10^{-08}$	$-9.56\cdot10^{-08}$	$-6.95\cdot10^{-08}$	$-6.45\cdot10^{-08}$	$-8.81\cdot10^{-08}$	$-8.09\cdot10^{-08}$
R^2	0.998	0.997	0.997	0.998	0.998	0.971
χ^2	$5.67\cdot10^{-4}$	$5.95\cdot10^{-4}$	$6.29\cdot10^{-4}$	$4.15\cdot10^{-4}$	$3.56\cdot10^{-4}$	$8.43\cdot10^{-3}$
SSD30						
k_0 (Pa·s^n)	1.92	2.60	2.45	1.69	0.766	0.645
k_1 (Pa·s^n· bar^{-1})	$-1.74\cdot10^{-05}$			$-1.23\cdot10^{-06}$		$-2.45\cdot10^{-06}$
n_0	$7.58\cdot10^{-02}$	$1.38\cdot10^{-02}$	$1.00\cdot10^{-02}$	$2.02\cdot10^{-02}$	$4.15\cdot10^{-02}$	$2.87\cdot10^{-02}$
n_1 (bar^{-1})	$5.52\cdot10^{-06}$			$7.22\cdot10^{-06}$		$3.12\cdot10^{-06}$
η_∞ (Pa·s)	3.92^{-02}	$2.30\cdot10^{-02}$	$1.55\cdot10^{-02}$	$1.19\cdot10^{-02}$	$9.69\cdot10^{-03}$	$7.39\cdot10^{-03}$

β_0 (bar)	$1.24 \cdot 10^{-03}$	$1.17 \cdot 10^{-03}$	$1.12 \cdot 10^{-03}$	$1.04 \cdot 10^{-04}$	$9.95 \cdot 10^{-04}$	$9.00 \cdot 10^{-04}$
β_1 (bar^{-2})	$-6.52 \cdot 10^{-08}$	$-7.41 \cdot 10^{-08}$	$-8.74 \cdot 10^{-08}$	$-8.51 \cdot 10^{-08}$	$-9.04 \cdot 10^{-08}$	$-7.67 \cdot 10^{-08}$
R^2	0.997	0.994	0.992	0.998	0.998	0.971
χ^2	$6.49 \cdot 10^{-4}$	$1.1 \cdot 10^{-3}$	$1.44 \cdot 10^{-3}$	$4.15 \cdot 10^{-4}$	$3.56 \cdot 10^{-4}$	$8.43 \cdot 10^{-3}$
SSH30						
k_0 ($Pa \cdot s^n$)	1.380	1.120	0.640	0.507	0.198	0.087
k_1 ($Pa \cdot s^n \cdot bar^{-1}$)	$-8.55 \cdot 10^{-06}$			$-2.50 \cdot 10^{-06}$		$-1.41 \cdot 10^{-06}$
n_0	$5.30 \cdot 10^{-02}$	$7.82 \cdot 10^{-02}$	$4.92 \cdot 10^{-02}$	$4.35 \cdot 10^{-02}$	$15.6 \cdot 10^{-02}$	$8.69 \cdot 10^{-02}$
n_1 (bar^{-1})	$5.7 \cdot 10^{-06}$			$4.69 \cdot 10^{-06}$		$4.76 \cdot 10^{-06}$
η_∞ (Pa·s)	$4.13 \cdot 10^{-02}$	$2.41 \cdot 10^{-02}$	$1.57 \cdot 10^{-02}$	$1.09 \cdot 10^{-02}$	$6.76 \cdot 10^{-03}$	$5.52 \cdot 10^{-03}$
β_0 (bar)	$1.24 \cdot 10^{-03}$	$1.07 \cdot 10^{-03}$	$1.03 \cdot 10^{-03}$	$9.87 \cdot 10^{-04}$	$9.06 \cdot 10^{-04}$	$8.91 \cdot 10^{-04}$
β_1 (bar^{-2})	$-7.72 \cdot 10^{-08}$	$-4.55 \cdot 10^{-08}$	$-6.35 \cdot 10^{-08}$	$-7.86 \cdot 10^{-08}$	$-7.80 \cdot 10^{-08}$	$-7.76 \cdot 10^{-08}$
P_r (bar)	1.0	1.0	1.0	1.0	1.0	1.0
R^2	0.997	0.997	0.997	0.994	0.993	0.990
χ^2	$6.07 \cdot 10^{-4}$	$7.11 \cdot 10^{-4}$	$8.07 \cdot 10^{-4}$	$1.42 \cdot 10^{-3}$	$1.64 \cdot 10^{-3}$	$2.36 \cdot 10^{-3}$

The shear sensitivity of these OSep dispersions in vegetable oil decreases slightly with pressure. Firstly, at lower shear rates, the shear stress decreases approaching a limit beyond the experimental windows, as suggested by the negative value of the k_1 parameter. Therefore, the consistency index decreases with increasing pressure at a constant temperature for all temperatures tested. Secondly, there is a slight increase in the flow index with pressure (positive value of parameter n_1), leading to an increased slope of the shear stress curve with pressure, as seen in Figure 8. Similar behavior has been observed for mineral oil-based drilling fluids formulated with organobentonites (Hermoso et al., 2014a), suggesting that the effect of the interactions between the particles in the dispersion is more evident at low temperatures and high pressures.

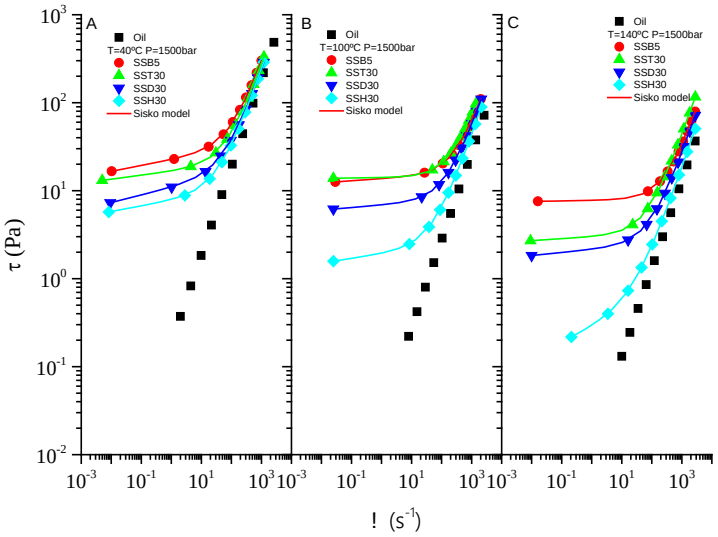

480

481 Figure 9. Steady state flow curves, at a pressure of 1500 bar, as a function of temperature,
482 for OBDF formulated with 3 m% of OSep. A) 40ºC; B) 100ºC; C) 140ºC.

483

484 Figure 10 shows the viscosity-pressure behavior, at high circulating shear rates (10^3-10^4
485 s^{-1}) measured in capillary flow. The isothermal viscosity at high shear rates exponentially
486 increases with pressure, with progressive negative deviation at higher pressure.
487 Therefore, the one-parameter-Barus model leads to an overestimation of the effect at
488 higher pressure which can be corrected by including a quadratic parameter β_1 (see Table
489 6). As expected, the Barus model parameters decrease with the increase in temperature.
490 Therefore, the viscosity-pressure-temperature behavior over the entire range of tested
491 temperatures and pressures can be modelled with a VFT equation:

492 $$\eta = A \cdot exp\left(\frac{(B+b_1(P-P_r)+b_2(P-P_r)^2)}{(T-T_r)-C}\right) \qquad (7)$$

493 The values of the parameters for the samples analyzed are summarized in Table 7. The
494 VFT equation is a valuable engineering tool for generalizing the viscosity-pressure-
495 temperature behavior over a wide temperature and pressure range (Hermoso et al., 2014a;
496 2017; Martín-Alfonso et al., 2021a; c).

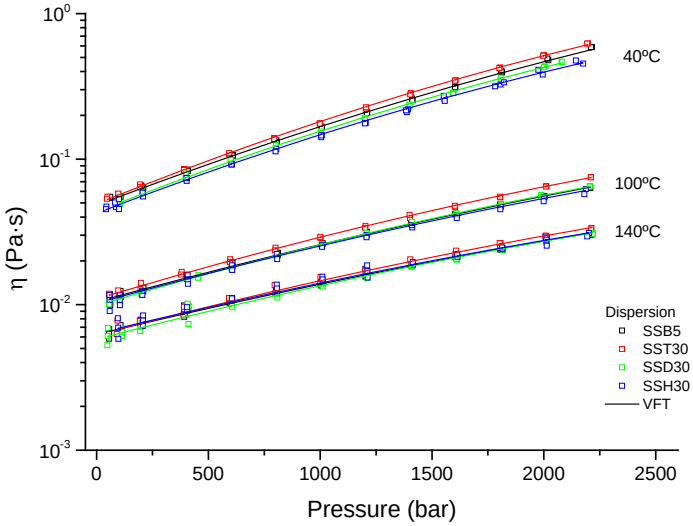

497

498 Figure 10. Viscosity-pressure curves, as a function of temperature, for OBM formulated
499 with 3 m% of OSep.

500

501 In the high shear rate region, the effect of pressure on the viscosity of these OSep
502 dispersions is very similar to that of the continuous phase of Newtonian vegetable oil.
503 The influence of the dispersed phase on viscosity is less significant at high pressures and
504 the dispersion-oil viscosity ratio decreases slightly with pressure, indicating a lower
505 contribution to bulk viscosity of the interactions in OSep and oil in the dispersed phase.
506 This is due to the increased viscosity of the continuous phase under pressure.
507 Furthermore, the increase in relative viscosity is also dampened at higher pressures. This
508 behavior has been previously reported for organobentonite dispersions (Hermoso et al.,
509 2014a), where the viscosity-pressure behavior at a high shear rate depends mainly on the
510 piezoviscous properties of the continuous phase, with a decreased influence of the
511 dispersed phase.

512

513 Table 7. Parameters of the modified VTF model for the analyzed samples.

	Vegetable oil	SSB5	SST30	SSD30	SSH30
A (Pa·s)	$1.48 \cdot 10^{-04}$	$1.64 \cdot 10^{-04}$	$3.17 \cdot 10^{-04}$	$3.44 \cdot 10^{-04}$	$5.96 \cdot 10^{-04}$
B (ºC)	875.3	1017.0	746.3	695.2	543.2
C (ºC)	-168.1	-179.1	-150.4	-146.9	-130.1
b_1 (ºC·bar^{-1})	0.247	0.239	0.223	0.217	0.183
b_2 (ºC·bar^{-2})	$-2.21 \cdot 10^{-05}$	$-1.87 \cdot 10^{-05}$	$-1.92 \cdot 10^{-05}$	$-2.03 \cdot 10^{-05}$	$-1.52 \cdot 10^{-05}$
P_r (bar)	1.0	1.0	1.0	1.0	1.0
T_r (ºC)	40.0	40.0	40.0	40.0	40.0
R^2	0.998	0.994	0.994	0.996	0.991
X^2	$9.03 \cdot 10^{-4}$	$2.49 \cdot 10^{-3}$	$2.33 \cdot 10^{-3}$	$1.60 \cdot 10^{-3}$	$3.51 \cdot 10^{-3}$

4 Conclusions

The organic modification of Sep at high-shear processing maintains the fibrous structure with a low degree of aggregation without altering the clay's crystalline structure. The amorphous adsorption of the organic surfactants on the surface is the dominant mechanism of the modification, with no apparent influence of the alkylammonium chain length. However, the degree of adsorption and thermal resistance of the surfactant are higher for surfactants with longer alkyl chains. The adsorption preferably takes place on the channels of Sep with no clear evidence of penetration into the tunnels.

Thermal properties of OBDFs formulated with OSep and vegetable depend primarily on the properties of the continuous oil phase, but are also influenced by interactions between the oil and the OSep in the dispersed phase, with a mass loss less than 1% at 300ºC. These OSep dispersions develop a fibrous structure without reaching an apparent yield stress. The structure maintains the pseudoplastic behavior in a wide range of shear rates,

temperatures and pressures, revealing a suitable rheology for the development of environmentally-friendly drilling fluids formulations. The viscous flow behavior can be suitably modelled by a factorial Sisko model. Pseudoplasticity remains relatively constant in dispersions SSB5, SST30, and SSD30, or decreases in dispersion SSH30 as temperature increases. The effect of pressure on pseudoplasticity is minimal. The relative viscosity dispersion/oil increases with temperature more significantly for OSep modified with surfactants with longer alkyl chains SH30 (from 1.47 to 1.62 in the range 40-140ºC at 1 bar). The relative viscosity is dampened at higher pressures (from 1.33 to 1.48 in the range 40-140ºC at 1500 bar), given the lower relative contribution of the interactions in the dispersed phase to the dispersion's bulk properties.

CRediT authorship contribution statement

M.J. Martín-Alfonso: Investigation, Resources, Writing – original draft, Visualization. A. Mejía: Conceptualization, Investigation, Resources. F.J. Martínez-Boza: Conceptualization, Formal analysis, Writing – review & editing, Funding acquisition, Supervision. P. Partal: Formal analysis, Project administration, Funding acquisition.

Declaration of Competing Interest

All authors declare that they have no conflicts of interest.

Data availability

Data will be made available on request.

Acknowledgements

This work was supported by the FEDER grants P18-RT-4684, PID2020-116905RB-I00 and MCIN/AEI/ 10.13039/501100011033.

Symbols

552	τ	Shear stress (Pa)
553	$\dot{\gamma}$	Shear rate (s^{-1})
554	τ_B	Bingham yield stress (Pa)
555	τ_H	Herschel-Bulkley yield stress (Pa)
556	η	Viscosity (Pa·s)
557	η_P	Plastic viscosity (Pa·s)
558	η_∞	High-shear-limiting-viscosity (Pa·s)
559	k_0	Consistency index ($Pa \cdot s^n$)
560	k_1	Pressure parameter of the consistency index ($Pa \cdot s^n \cdot bar^{-1}$)
561	n_0	Flow index
562	n_1	Pressure parameter of the flow index (bar^{-1})
563	β_0	Linear piezoviscous coefficient (bar^{-1})
564	β_0	Quadratic piezoviscous coefficient (bar^{-2})
565	A	VFT preexponential parameter (Pa·s)
566	B	VFT B parameter (ºC)
567	C	VFT C parameter (ºC)
568	b_1	VFT b1 parameter ($ºC \cdot bar^{-1}$)
569	b_2	VFT b2 parameter ($ºC \cdot bar^{-2}$)
570	T	Temperature (ºC)
571	P	Pressure (bar)
572	T_r	Temperature of reference (ºC)
573	P_r	Pressure of reference (bar)
574	R^2	Regression coefficient

575 χ^2 Reduced Chi-square

576

577 # References

578 Abdo, J., Al-Sharji, H., Hassan, E., 2016. Effects of nano-sepiolite on rheological
579 properties and filtration loss of water-based drilling fluids. Surf. Interface Anal. 48, 522–
580 526. https://doi.org/10.1002/sia.5997.

581 Adhvaryu, A., Erhan, S., Perez, J., 2002. Wax appearance temperatures of vegetable oils
582 determined by differential scanning calorimetry: effect of triacylglycerol structure and its
583 modification. Thermochim. Acta. 395 (1), 191–200. https://doi.org/10.1016/S0040-
584 6031(02)00180-6.

585 Agwu, O.E., Akpabio, J.U., Ekpenyong, M.E., Inyang, U.G., Asuquo, D.E., Eyoh, I.J.,
586 Adeoye, O.S., 2021. A critical review of drilling mud rheological models. J. Pet. Sci. Eng.
587 203, 108659. https://doi.org/10.1016/j.petrol.2021.108659.

588 Agwu, O.E., Okon, A.N., Udoh, F.D., 2015. A comparative study of diesel oil and
589 soybean oil as oil-based drilling mud. J. Petrol. Eng. 828451.
590 https://doi.org/10.1155/2015/828451.

591 Ahmed, A., Elkatatny, S., Al-Afnan, S., 2021. Applications of Biodiesel in Drilling
592 Fluids. Geofluids, 5565897. https://doi.org/10.1155/2021/5565897.

593 Alvarez Berenguer, A., Perez Castells, R., Aragon Martinez, J.J., Esteban Aldezabal,
594 M.A., 1985. A Rheological Grade Sepiolite Product and Processes for Its Manufacture.
595 European Patent EP0170299.

596 Amani, M., Al-Jubouri, M., Shadravan, A., 2012. Comparative study of using oil-based
597 mud versus water-based mud in HPHT fields. Adv. Petrol. Explorat. Develop. 4 (2), 18–
598 27. https://doi.org/10.3968/j.aped.1925543820120402.987.

599 Aranda, P., Kun, R., Martín-Luengo, M.A., Letaïef, S., Dékány, I., Ruiz-Hitzky, E., 2008.
600 Titania-sepiolite nanocomposites prepared by a surfactant templating colloidal route.
601 Chem. Mater. 20, 84–89. https://doi.org/10.1021/cm702251f.

602 Aznar, A., Casal, B., Ruiz-Hitzky, E., Lopez-Arbeloa, I., Lopez-Arbeloa, F., Santaren, J.,
603 Alvarez, A. 1992. Adsorption of methylene blue on sepiolite gels: Spectroscopic and
604 rheological studies. Clay Minerals. 27(1), 101-108.
605 https://doi.org/10.1180/claymin.1992.027.1.10.

606 Bilgiç, C., 2005. Investigation of the factors affecting organic cation adsorption on some
607 silicate minerals. J. Colloid Interface Sci. 281, 33-38.
608 https://doi.org/10.1016/j.jcis.2004.08.038.

609 Caenn, R., Darley, H.C.H., Gray, G.R., 2017. Composition and Properties of Drilling
610 Fluids and Completion Fluids, seventh ed. Gulf Professional Publishing, Houston.

611 De Brito Buriti, B.M.A., Barsosa, M.E., Da Silva Buriti, J., De Melo Cartaxo, J., Ferreira,
612 H.S., Araujo Meves, G., 2022. Modification of palygorskite with cationic and nonionic
613 surfactants for use in oil-based drilling fluids. J. Therm. Anal. Calorim. 147, 2935–2945.
614 https://doi.org/10.1007/s10973-021-10701-w.

615 Ettehadi, A., Tezcan, M., Altun, G. 2020. Rheological behavior of water-clay suspensions
616 under large amplitude oscillatory shear. Rheol. Acta 59, 665–683.
617 https://doi.org/10.1007/s00397-020-01221-9.

618 Frost, R.L., Ding, Z., 2003. Controlled rate thermal analysis and differential scanning
619 calorimetry of sepiolites and palygorskites. Thermochim. Acta. 397 (1–2), 119–128.
620 https://doi.org/10.1016/S0040-6031(02)00228-9.

621 García-López, D., Fernández, J.F., Merino, J.C., Santarén, J., Pastor, J.M., 2010. Effect
622 of organic modification of sepiolite for PA 6 polymer/organoclay nanocomposites.

623 Compos. Sci. Technol. 70, 1429–1436.
624 https://doi.org/10.1016/j.compscitech.2010.05.020.

625 Hermoso, J., Martínez-Boza, F., Gallegos, C., 2014a. Influence of viscosity modifier
626 nature and concentration on the viscous flow behavior of oil-based drilling fluids at high
627 pressure. Appl. Clay Sci. 87, 14–21. https://doi.org/10.1016/j.clay.2013.10.011.

628 Hermoso, J., Martínez-Boza, F., Gallegos, C., 2014b. Combined effect of pressure and
629 temperature on the viscous behaviour of all-oil drilling fluids. Oil Gas Sci. Technol. 69
630 (7), 1283–1296. https://doi.org/10.2516/ogst/2014003.

631 Hermoso, J., Martínez-Boza, F., Gallegos, C., 2015. Influence of aqueous phase volume
632 fraction, organoclay concentration and pressure on invert-emulsion oil muds rheology. J.
633 Ind. Eng. Chem. 22, 341–349. https://doi.org/10.1016/j.jiec.2014.07.028.

634 Karataş, D., Tekin, A., Celik, M., 2013. Adsorption of quaternary amine surfactants and
635 their penetration into the intracrystalline cavities of sepiolite. New J. Chem.37, 3936–
636 3948. https://doi.org/10.1039/c3nj00752a.

637 Lagaly, G., Ogawa, M., Dekany, I., 2006. Clay mineral organic interactions. In: Bergaya,
638 F., Theng, B.K.G., Lagaly, G. (Eds.), Handbook of Clay Science. Developments in Clay
639 Science, 1. Elsevier, Amsterdam.

640 Li, W., Zhao, X., Ji, Y., Peng, H., Li, Y., Liu, L., Han, X., 2016. An investigation on
641 environmentally friendly biodiesel-based invert emulsion drilling fluid. J. Pet. Explor.
642 Prod. Technol. 6, 505–517. https://doi.org/10.1007/s13202-015-0205-7.

643 Ma, C., Wen, R., Zhou, F., Zhao, H., Bao, X., Evelina, A., Long, W., Wei, Z., Ma, L.,
644 Liu, J. 2022. Preparation and application of an environmentally friendly compound
645 lubricant based biological oil for drilling fluids. Arabian J. Chem. 15, 103610.
646 https://doi.org/10.1016/j.arabjc.2021.103610.

Martín-Alfonso, M.J., Mejía, A., Martínez-Boza, F.J., Martín-Alfonso, J.E., 2021a. Rheological characterization of sepiolite-vegetable oil suspensions at high pressures. Appl. Clay Sci. 212, 106220. https://doi.org/10.1016/j.clay.2021.106220.

Martín-Alfonso, M.J., Pozo, J., Delgado-Sánchez, C., Martínez-Boza, F.J., 2021c. Thermal and rheological properties of hydrophobic nanosilica in sunflower oil suspensions at high pressures. Nanomaterials, 11 (11), 3037. https://doi.org/10.3390/nano11113037.

Martín-Alfonso, M.J.; Martínez-Boza, F.J.; Navarro Dominguez, F.J.; Partal, P. 2021b. Device for Measuring Rheological Properties in Fluids. WO2020070359A1.

Mejía, A., García, N., Guzmán, J., Tiemblo, P., 2014. Surface modification of sepiolite nanofibers with PEG based compounds to prepare polymer electrolytes. Appl. Clay Sci. 95, 265–274. https://doi.org/10.1016/j.clay.2014.04.023.

Mohamed, A., Salehi, S., Ahmed, R., 2021. Significance and complications of drilling fluid rheology in geothermal drilling: a review. Geothermics. 93, 102066. https://doi.org/10.1016/j.geothermics.2021.102066.

Paswan, B.K., Mahto, V., 2020. Development of environment-friendly oil-in-water emulsion based drilling fluid for shale gas formation using sunflower oil. J. Petrol. Sci. Eng. 191, 107129. https://doi.org/10.1016/j.petrol.2020.107129.

Ratkievicius, L., Filho, F., Neto, E., Santanna, V., 2017. Modification of bentonite clay bya cationic surfactant to be used as a viscosity enhancer in vegetable-oil-based drilling fluid. Appl. Clay Sci. 135, 307–312. https://doi.org/10.1016/j.clay.2016.10.011.

Reinoso, D., Martín-Alfonso, M.J., Luckham, P.F., Martínez-Boza, F.J., 2019. Rheological characterisation of xanthan gum in brine solutions at high temperature. Carbohydr. Polym. 203, 103–109. https://doi.org/10.1016/j.carbpol.2018.09.034.

671 Reinoso, D., Martín-Alfonso, M.J., Luckham, P.F., Martínez-Boza, F.J., 2020. Flow
672 behavior and thermal resistance of xanthan gum in formate brine. J. Pet. Sci. Eng.188,
673 106881. https://doi.org/10.1016/j.petrol.2019.106881.

674 Rossi S., Luckham P.F., Tadros Th.F., 2002. Influence of nonionic polymers on the
675 rheological behavior of Na+-montmorillonite clay suspensions–I Nonyphenol–
676 polypropylene oxide –polyethylene oxide copolymers. Colloids Surf. A. 201, 85-100.
677 https://doi.org/10.1016/S0927-7757(01)00792-0.

678 Ruiz-Hitzky, E., 2001. Molecular access to intracrystalline tunnels of sepiolite. J. Mater.
679 Chem. 11 (1), 86–91.

680 Rytwo, G., Nir, S., Margulies, L., Casal, B., Merino, J., Ruiz-Hitzky, E., Serratosa, J.M.,
681 1998. Adsorption of monovalent organic cations on sepiolite: Experimental results and
682 model calculations. Clay Clay Miner. 46, 340–348.
683 https://doi.org/10.1346/CCMN.1998.0460313.

684 Serratosa, J.M., 1979. Surface Properties of Fibrous Clay Minerals (Palygorskite and
685 Sepiolite). In: Mortland, M.M., Farmer, V.C. (Eds.), Developments in Sedimentology.
686 Elsevier, Amsterdam, pp. 99-109.

687 Shariatmadari, H., Mermut, A.R., Benke, M.B., 1999. Sorption of Selected Cationic and
688 Neutral Organic Molecules on Palygorskite and Sepiolite. Clays Clay Miner. 47, 44–53.
689 https://doi.org/10.1346/CCMN.1999.0470105.

690 Sulaimon, A.A., Adeyemi, B.J., Rahimi, M., 2017. Performance enhancement of selected
691 vegetable oil as base fluid for drilling HPHT formation. J. Pet. Sci. Eng. 152, 49–59.
692 http://dx.doi.org/10.1016/j.petrol.2017.02.006.

693 Tapavicza, S.V., 2005. Vegetable esters make drilling fluids more environmentally
694 friendly. Oil and Gas J. 103, 22.

Tartaglione, G., Tabuani, D., Camino, G., Moisio, M., 2008. PP and PBT composites filled with sepiolite: Morphology and thermal behaviour. Compos. Sci. Technol. 68, 451–460. https://doi.org/10.1016/j.micromeso.2007.04.020.

Tiemblo, P., García, N., Hoyos, M., Mejía, A., de Francisco, R., 2015. In: Aliofkhazraei, M. (Ed.), Organic Modification of Hydroxylated Nanoparticles: Silica, Sepiolite, and Polysaccharides, in Handbook of Nanoparticles. Springer International Publishing, New York, pp. 1–35.

Tunç, S., Duman, O., Cetinkaya, A., 2011. Electrokinetic and rheological properties of sepiolite suspensions in the presence of hexadecyltrimethylammonium bromide. Colloids Surf. A Physicochem. Eng. Asp. 377, 123–129. https://doi.org/10.1016/j.colsurfa.2010.12.036.

Tunç, S., Duman, O., Kanci, B., 2012. Rheological measurements of Na-bentonite and sepiolite particles in the presence of tetradecyltrimethylammonium bromide, sodium tetradecyl sulfonate and Brij 30 surfactants. Colloids Surf. A Physicochem. Eng. Asp. 398, 37–47. https://doi.org/10.1016/j.colsurfa.2012.02.006.

Weng, J., Gong, Z., Liao, L., Lv, G., Tan, J., 2018. Comparison of organo-sepiolite modified by different surfactants and their rheological behavior in oil-based drilling fluids. Appl. Clay Sci. 159, 94–101. https://doi.org/10.1016/j.clay.2017.12.031.

Yan, K., Guo, Y., Wu, X., Cheng, F., 2016. Effect of organic matter on the Rietveld quantitative analysis of crystalline minerals in coal gangue. Powder Diffract. 31, 185–191. https://doi.org/10.1017/S088571561600018X.

Zhang, J.R., Xu, M.D., Christidis, G.E., Zhou, C.H., 2020. Clay minerals in drilling fluids: functions and challenges. Clay Miner. 55, 1–11. https://doi.org/10.1180/clm.2020.10.

719 Zhuang, G., Wu, H., Zhang, H., Zhang, Z., Zhang, X., Liao, L., 2017. Rheological
720 properties of organo-palygorskite in oil-based drilling fluids aged at different
721 temperatures. Appl. Clay Sci. 137, 50–58. https://doi.org/10.1016/j.clay.2016.12.015.

722 Zhuang, G., Zhang, Z., Yang, H., Tan, J., 2018a. Structures and rheological properties of
723 organo-sepiolite in oil-based drilling fluids. Appl. Clay Sci. 154, 43–51.
724 https://doi.org/10.1016/j.clay.2017.12.048.

725 Zhuang, G., Zhang, Z., Chen, H., 2018b. Influence of the interaction between surfactants
726 and sepiolite on the rheological properties and thermal stability of organo-sepiolite in oil-
727 based drilling fluids. Microporous Mesoporous Mater. 272, 143–154.
728 https://doi.org/10.1016/j.micromeso.2018.06.017.

729 Zhuang, G., Zhang, Z., Peng, S., Gao, J., Jaber, M., 2018c. Enhancing the rheological
730 properties and thermal stability of oil-based drilling fluids by synergetic use of organo-
731 montmorillonite and organo-sepiolite. Appl. Clay Sci. 161, 505–512.
732 https://doi.org/10.1016/j.clay.2018.05.018.

733 Zhuang, G., Zhang, Z., Jaber, M., 2019. Organoclays used as colloidal and rheological
734 additives in oil-based drilling fluids: an overview. Appl. Clay Sci. 177, 63–81.
735 https://doi.org/10.1016/j.clay.2019.05.006.